communications physics

A Nature Portfolio journal

Article

https://doi.org/10.1038/s42005-026-02551-5

Structure and polydispersity of single lipid vesicles by small-angle X-ray scattering at European XFEL

Charlotte Neuhaus[1], Moritz L. Stammer[1], Jette Alfken[1], Markus Osterhoff[1], Karlo Komorowski[1], András Major[1], Johan Bielecki[2], Safi Rafie-Zinedine[2], Raphael de Wijn[2], Romain Letrun[2], Juncheng E[2], Richard Bean[2] & Tim Salditt[1] ✉

Structure analysis of supra-molecular assemblies is of considerable interest in a wide range of research fields, but also extremely challenging. Biomolecular colloidal particles, such as biological vesicles or small unilamellar lipid vesicles, for example, measure only a few tens of nanometers, and need to be probed in hydrated and functionalized environments. Small-angle X-ray scattering (SAXS) is a well established technique offering high resolution in solution and at room temperature. However, due to the average over an extremely large ensemble, SAXS yields information only about the average structure (size and electron density profile). Many structural details are lost or screened by polydispersity, as well as by powder averaging. To overcome these limitations, we study single vesicles sequentially by coherent diffractive X-ray imaging using femtosecond X-ray free-electron laser (XFEL) pulses. For these experiments, single vesicles surrounded by a thin water layer are delivered into a nano-focused XFEL beam by an aerosol injector. Following the 'diffract-before-destroy' principle, the individual vesicles are probed on time scales where radiation damage has not yet set in. This approach leads to the measurement of thousands of diffraction patterns that can now be analyzed without limits associated with ensemble averaging.

Starting with the first X-ray diffraction experiments from liquids by Peter Debye and Paul Scherrer[1] more than hundred years ago, non-crystallographic structure analysis by diffraction has become an enabling tool for physical chemistry, materials science, supra-molecular chemistry, pharmacology, and biochemistry. Small-angle X-ray scattering (SAXS), in particular, provides structural and dynamic insights into soft-matter complexes, macromolecules, and biomolecular assemblies, under near-native conditions. The electron density distribution on larger scale can be derived without any need for labeling, under conditions compatible with a wide range of complex chemical environments[2–5]. The capability to probe supra-molecular structure and assembly based on quantitative modeling also at room temperature and in solution represents an essential asset for many applications in biochemistry, molecular biology and physical chemistry. Based on these properties, SAXS remains relevant even after the emergence of novel powerful real-space microscopic techniques such as cryo electron microscopy (cryo-EM) and super-resolution optical fluorescence microscopy.

Self-assembly of amphiphilic molecules is at the base of a wide range of supra-molecular materials[6–8] and cellular compartmentalization[9]. The ability to form many different structures, often also denoted as lipid polymorphism, and the functional responsiveness of lipid assemblies to solution properties have fascinated researchers for a long time. Lipid vesicles (LVs) of different size and shapes, for example, are used as smart materials in drug delivery, cosmetics, or as biosensors. Vesicles with a rich inventory of lipids and proteins, for example, support a wide range of metabolic functions, including protein secretion, hormone release, neurotransmitter transmission, and waste removal, just to name a few. Solution scattering with X-rays (SAXS) and neutrons (SANS) has contributed to a quantitative understanding of vesicle structure[10–13], assembly[8,14], interactions[15,16], and phase transitions[17,18].

But non-crystallographic structure analysis by diffraction comes at a price: as an ensemble technique, it typically requires large volumes of the analyte, homogeneous structure, and is also associated with an information loss due to random orientations and polydispersity. These effects screen

---

[1]Institut für Röntgenphysik, Georg-August-Universität Göttingen, Göttingen, Germany. [2]SPB/SFX, European XFEL, Schenefeld, Germany.
✉e-mail: tsaldit@gwdg.de

many of the detailed structural parameters, in particular of multi-component systems. Considering again vesicles as an example, they may contain many different lipid and protein species, and vary in size and shape. The structural heterogeneity is shared with other biomolecular and supramolecular systems, and represents a biologically relevant property by itself, which can for example inform on the robustness of a biological function, the yield of a synthetic pathway, or the effectiveness of purification. The advent of high brilliance synchrotron radiation, in particular of the third and fourth generation light sources, has substantially elevated the capabilities of SAXS, in particular by extending the resolution, reducing the minimum concentration and volume, but at the same time has aggravated the risks of radiation damage. At the same time, a typical SAXS experiment still requires a macroscopic ensemble average, for example on the order of 10^{10} lipid vesicles in[15]. All structural parameters reported are hence averages over such an ensemble. Serial acquisitions with nano-focused synchrotron radiation and microfluidic sample delivery can help to probe smaller and less contaminated ensembles of biological particles, but not at the single particle level. Furthermore, radiation damage in the highly focused beams would be prohibitive[19].

Contrarily, radiation damage is outrun by the ultrashort pulse length of X-ray free-electron laser (XFEL) radiation, based on the *diffract-before-destroy* principle[20,21]. The vision of single particle diffractive imaging by inversion of the coherent diffraction data has been a large science driver for the development of XFEL sources, see refs. 22,23, for reviews of the state-of-the-art. The rationale of single particle coherent diffractive imaging (CDI) was to also get rid of the model-based analysis, another property inherent in all classical diffraction experiments, and to directly invert the diffraction pattern. As was first shown with synchrotron radiation in ref. 24, and later for single XFEL pulses in ref. 21, it is possible to invert a coherent diffraction pattern directly by phase retrieval[25], based on more or less mild priors or constraints, such as compact support, range constraints of electron density, or sparseness, for example. More recently, the inversion approach has been extended to cases of multiple identical particles in the beam, exploiting speckle contrast (so-called fluctuation scattering)[26]. Apart from constraints, direct inversion, however, requires stringent sampling constraints in the detection plane, oftentimes not available experimentally, for example due to limitations of current detector pixel size and inter-module gaps for single pulse acquisition. To this end, substantial instrumental efforts have been invested in sources and beamlines, for example at the 'Single Particle Diffraction' instrument of the European XFEL[27,28], as well as in sample delivery by aerosol electrospray methods[29], and finally the development of data analysis. Starting from the first demonstration of single particle imaging in two dimensions (2D) shown for the mimivirus[30], and the first 3D reconstructions[31], to heterogeneous serial ensembles of small cell organelles[32], the field is now reaching the level of single proteins[33–37]. The reconstruction of a diffracting particle in three dimensions (3D) has been a particular challenge, and requires thousands of diffraction patterns obtained from identical particles probed in random orientations, which can be recovered from a sophisticated Bayesian analysis[38,39].

In this work we adopt a different approach, exploiting at the same time the power of single particle coherent diffraction with femtosecond XFEL pulses, as well as of model-based analysis and signal accumulation by radial averaging. We thus bring SAXS to the level of a single particle (SP) probe. We use this SP-SAXS approach, to probe single lipid vesicles individually by diffraction, and at high throughput based on sequential injection and high repetition rate. With respect to conventional SAXS, this leads to a reduction of scattering particles, contributing to a single diffraction pattern by 10 orders of magnitude! In contrast to the CDI examples mentioned above, we deduce structural properties by classical model-based diffraction analysis, rather than by model-free inversion of the data, which failed under given conditions of size, scattering strength, and detector gaps. Using the robustness of least-square fitting with a well-justified structural model, we can deduce i.e. radius R, ellipticity ε, and electron density profile $\rho(r)$ from a single diffraction pattern. Due to the priors inherent in the model as well as the signal accumulation resulting from azimuthal averaging, this SP-SAXS approach can exploit diffraction data at higher q compared to CDI. Based on the ultrashort XFEL pulse duration[20,21], this is possible at the single vesicle level, unaffected by radiation damage. Histogramming structural parameters for the sequential stream of vesicle data, we can overcome the main limitation of conventional solution SAXS, which is associated with polydispersity and loss of information by ensemble averaging.

While model-free determination of a 3D structure directly from the diffraction patterns by phase retrieval remains perhaps the most general approach, it requires a stream of $10^4 - 10^6$ identical particles, which is not possible for many applications, such as the vesicles studied here. As in studies of serial femtosecond crystallography, i.e. crystallography based on sequential injection of nano-crystal, as well as in SAXS of smaller ensembles of identical macromolecules injected by a liquid jet into a XFEL beam[40], our work shows that model based diffraction analysis should not be superseded. While the CDI approach is limited to identical or nearly-identical particles, model diffraction analysis can analyze non-invertible data, without the need to accumulate the signal from many shots, and is much more robust with regard to sampling issues and detector technology. Moreover, the priors inherent in the model can be leveraged, and the model can be formulated directly in 3D, even if the data is only 2D. As we highlight for the example of vesicles, relevant structural data can be derived from model fitting of single diffraction patterns, in particular after slight signal accumulation by radial averaging, arriving at the same data structure as in classical SAXS, but now for a single particle. By extreme concentration of photons both spatially and temporally, the scattering signal can be increased without being affected by radiation damage.

Methods

Experimental concept

Experiments were carried out at the Single Particles, Clusters, and Biomolecules and Serial Femtosecond Crystallography (SPB/SFX) instrument[28] of the European XFEL in Hamburg, Germany. Figure 1 presents the setup, with a schematic of the SPB beamline with SASE 1 undulator[41], focusing mirrors, sample injector, and the detector, as well as schematics of the timing scheme and aerosol injection. The experimental parameters are tabulated in Table 1. The electron accelerator and SASE1 undulator were operated to deliver femtosecond X-ray pulses with a photon energy of $E_{ph} = 6$ keV and an average pulse energy of $E_{pulse} \approx (2.9 - 3.15)$ mJ. A timing scheme with 10 Hz pulse trains, each with 352 pulses, was used as visualized in Fig. 1 (c). The average pulse energy of each pulse was determined by an X-ray Gas Monitor (XGM)[42]. The beam was focused by Kirkpatrick-Baez mirrors (KB mirrors) to a size of 300×300 nm^2. The aperture in front of the KB was opened to 3.5×3.5 mm^2. Vesicles were prepared from different lipids. Here we show results for 1:1 mixtures of DOPS (1,2-di-(9Z-octadecenoyl)-sn-glycero-3-phospho-L-serine) and DOPC (1,2-di-(9Z-octadecenoyl)-sn-glycero-3-phosphocholine) at a lipid concentration of 10 mM, purchased from Avanti Polar Lipids (Alabaster, Al, USA) in ultrapure water, see Supplementary Note 1.1 for details on preparation. Vesicles were injected into the beam as droplets using the Uppsala Aerosol Injector as described in ref. 29, which is illustrated in Fig. 1 (d-f). Isolated water droplets containing single vesicles were formed by an electrospray nebulizer. Excess water was evaporated by inert gas (N_2, CO_2), leaving behind isolated vesicles, surrounded by a thin layer of water. The integrity of the vesicles during aerosolization is key to the present method. The concept is based on evaporational cooling after rapid injection into vacuum which vitrifies the particle with its native hydration shell. For this reason, aerosolized particles are considered to be much closer to the physiological state than a counterpart which would be dehydrated by a conventional drying process. Apart from the SAXS results themselves which offer a *a posteriori* confirmation that the vesicles are not collapsed or ripped apart, the injection parameters and the size distribution were also controlled before the beamtime by differential mobility measurements. The particle beam was focused by an aerodynamic lens stack, leading to a waist size of the particle beam estimated to $\approx (30 - 50)\,\mu$m. Due to this small size, a high

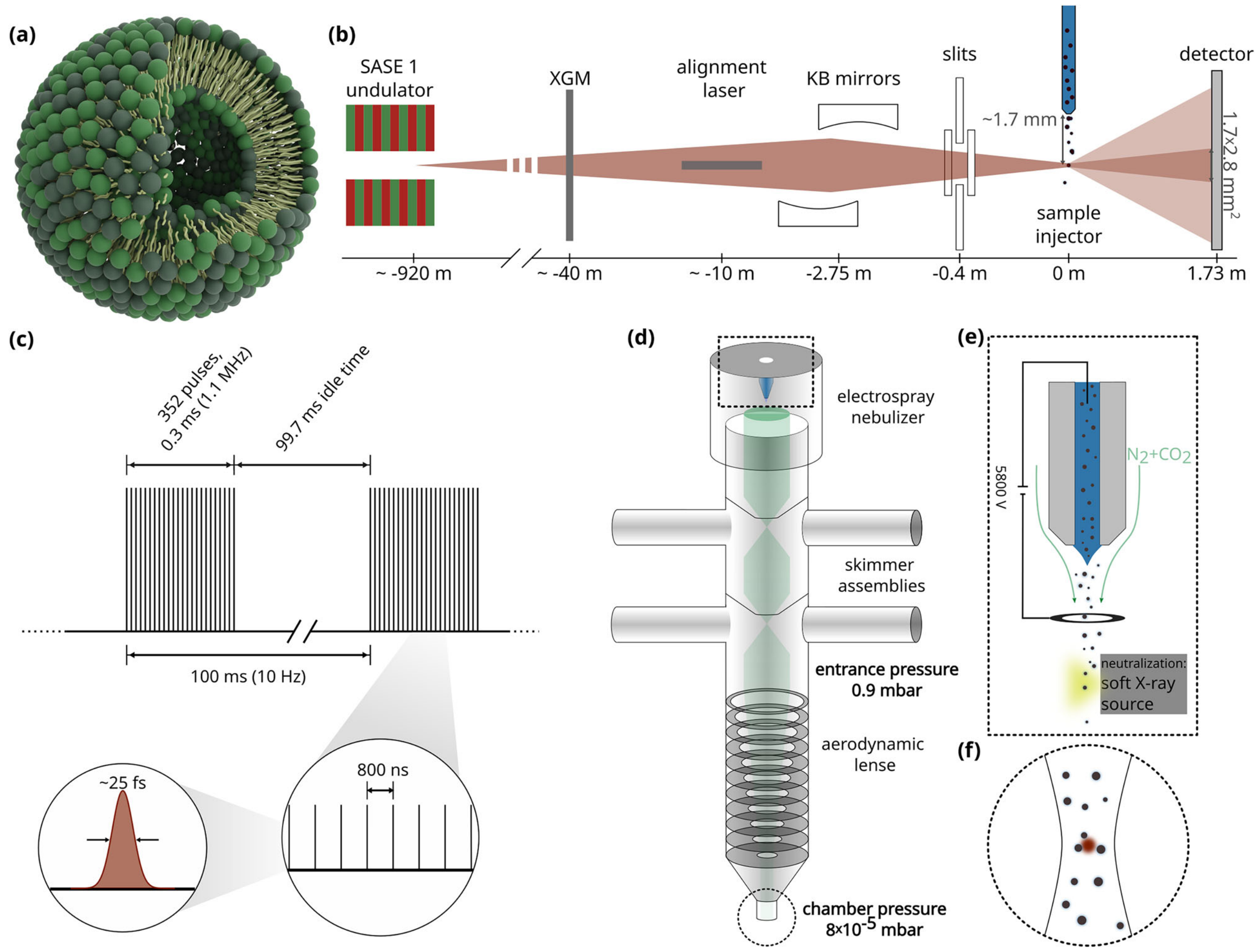

Fig. 1 | Instrumentation of single vesicle SAXS. **a** Rendering of a two component unilamellar lipid vesicle. Note that while the bilayer thickness corresponds to about $\simeq 3.5$ nm, the radius R is not sketched to scale and smaller that most of the of vesicles probed. **b** Schematic of the SPB beamline[28] used for the experiments. The SASE1 undulator delivers a pulsed X-ray beam and the average energy of each pulse is determined using an X-ray Gas Monitor (XGM)[42]. The beam is focused to a size of FWHM = 300 nm using two Kirkpatrick-Baez-mirrors (KB mirrors), followed by vertical and horizontal slits to clean up the beam. Single vesicles are delivered into the beam by the Uppsala Aerosol Injector (illustrated in d-f) and the diffracted signal is measured by the AGIPD 1M detector[43] at a distance of 1.73 m behind the sample. The primary beam has a size of $1.7 \times 2.8\ \mathrm{mm}^2$ in the detector plane. **c** Schematic of the time structure of the European XFEL modified from[51]. The 25 fs X-ray pulses are organized in trains of 352 pulses, with an intra-train repetition rate of 1.1 MHz. The trains arrive at a repetition rate of 10 Hz. The insets show (right) the 800 ns spacing of pulses within a train, and (left) the width of a single pulse. **d** Schematic of the Uppsala aerosol injector used to create isolated single particles. The electrospray nebulizer aerosolizes the vesicles from solution by applying an electric field between the capillary and a ring-electrode. This leads to the formation of a stable Taylor cone resulting in the formation of solvent droplets containing single vesicles. A mixture of CO_2 and N_2 is used to prevent electric discharge. This process is shown in (**e**) in more detail. The charged particles are neutralized using a soft X-ray source (Hamamatsu L12645). Note that this soft X-ray source in the sketch is not to be confused with the XFEL beam positioned further below. Excess water around the vesicles is evaporated by differential pressure gradient in the skimmer assembly and the particle beam is focused by an aerodynamic lens. The produced particle beam is illustrated in (**f**). The beam follows the Gaussian beam model and has a size estimated to about $(30 - 50)\ \mu\mathrm{m}$, the estimate for the speed of aerosolized vesicles is in the range of $v = 100\ \frac{\mathrm{m}}{\mathrm{s}}$[29,52,53].

Table 1 | Beamline settings and parameters

Parameter	Value
pulse energy (mJ)	2.9–3.1
photon energy (keV)	6
pulses/second	3520
pulse duration (fs)	25
beam size (FWHM) (nm^2)	300 × 300
detector	AGIPD 1M
detector distance (m)	1.73
pixel size (μm^2)	200 × 200
# pixel	1024 × 1024

particle density is achieved and the simultaneous arrival of a vesicle and the X-ray pulse in the interaction region (i.e. the spatio-temporal overlap) is more likely. The sample was continuously injected into the beam, and the diffraction signal was recorded by a 1 megapixel Adaptive Gain Integrating Pixel Detector (AGIPD 1M)[43] at a distance of 1.73 m behind the sample injection site. In the detection plane, the beam size was 1.7 mm(*hor.*) × 2.8 mm(*vert.*), corresponding to $q_{min} = 0.049\ \mathrm{nm}^{-1}$. Data was collected in runs of 5 minutes, resulting in 1056000 diffraction images per run. Several runs were collected on each sample.

To determine the diffraction patterns containing events with single vesicles in the beam, i.e. the so-called *hits*, a three-step hit-finding process was implemented. First, the normalized scattering intensity and the number of lit pixels were considered, and lower bounds for each were set. Second, only those diffraction patterns were kept which exhibited the characteristic maxima and minima of single vesicles, without signs of aggregation, such as

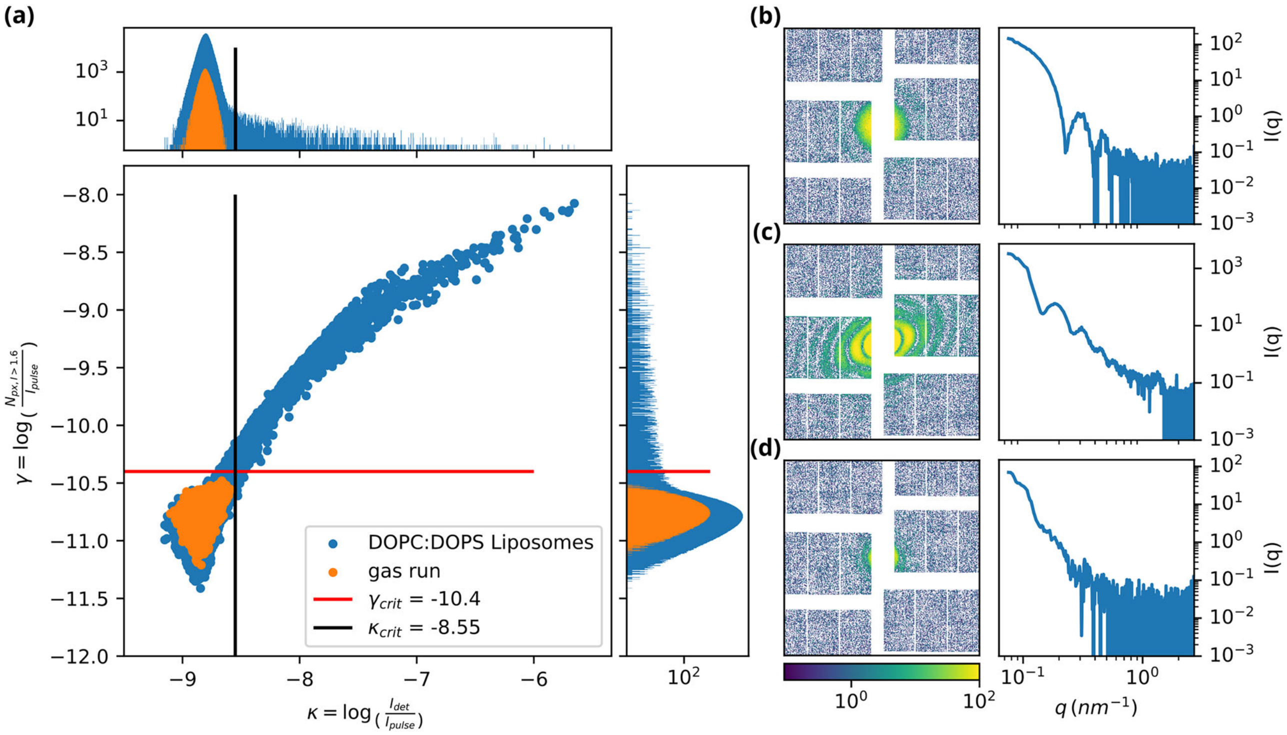

Fig. 2 | Hit-finding and data selection. a Normalized intensity $\kappa = \log\left(\frac{I_{\text{scattered}}}{I_{\text{pulse}}}\right)$ and the normalized number of lit pixels $\gamma = \log\left(\frac{N_{\text{px,I} > 1.6}}{I_{\text{pulse}}}\right)$ in the central two detector modules, for each shot in a run with DOPC:DOPS vesicles (blue) injected, compared to an empty gas run (orange). For normalization, the average pulse energy is calculated by an X-ray gas monitor upstream of the sample injection. The carrier gas was measured for a run time of 70.9 s, yielding $N \approx 250{,}000$ diffraction images. The liposome sample was measured for a run time of 309.1 s, yielding $N = 1088032$ diffraction images. For the sample presented here, the thresholds were set to $\gamma \geq -10.4$ and $\kappa \geq -8.55$, this corresponds to a hit rate of $\approx 0.2\%$ for all hits or a hit rate of $\approx 0.01\%$ for hits classified as good hits. (b-d) Diffraction patterns for different events (hits) and the corresponding azimuthal average: (**b**) a single vesicle, (**c**) multiple vesicles, and (**d**) a vesicle in the tail of the beam, with correspondingly much weaker scattering intensity.

a maximum in the high q-range. Finally, diffraction patterns with an anisotropy beyond elliptical shape were filtered out manually. Figure 2 illustrates the hit-finding results, with details and further graphics given in Supplementary Note 1.3. To determine the scattering background caused by the excess carrier gas (CO_2 and N_2) of the injector, empty carrier gas without vesicles was injected in the beam. The fitted curve of this data was subtracted from the azimuthally averaged curves as background before fitting the vesicle data. As an alternative scheme, the background scattering curve was computed from the 'misses' of the run, which essentially yielded an identical background curve.

The azimuthally averaged intensity curves of the single vesicle diffraction data is given by

$$I(q) = r_0 I_0 \Delta\Omega \rho_{\text{water}} \int_0^{2\pi} |F(q, R, \varepsilon, \theta, \varphi)|^2 \mathrm{d}\varphi\,, \tag{1}$$

with classical electron radius r_0, solid angle $\Delta\Omega$, and average electron density of water ρ_{water}. The form factor F is modeled for a vesicle deformed as a rotational ellipsoid (spheroid), with radius R, ellipticity ε, and a random orientation, parameterized by the angle θ between the ellipsoidal axis and the beam, and azimuthal angle φ, which is easily inferred from anisotropy in detector plane. The lipid bilayer is modeled in form of three Gaussians[44], parameterized in terms of excess scattering density ρ_h and ρ_t and width (standard deviation) σ_h and σ_t for the lipid head- and tail-regions, respectively, and bilayer thickness z_{hh}, defined as the distance between the headgroup maxima, associated with the phosphor group of /DOPC/DOPS. As shown in Fig. 3 which illustrates the fit model, the radius R is defined as the outer surface facing the vacuum, including a thin water layer of bound water with thickness ΔR between the outer leaflet and the droplet surface. σ denotes the surface roughness of the bound water layer. With these structural parameters, the form factor becomes

$$\begin{aligned} F \quad = \quad & 4\pi\varepsilon R^3 \frac{\sin\big(u(q,R) - u(q,R)\cos(u(q,R))}{(u(q,R))^3} e^{-\frac{\sigma^2 u(q,R)^2}{2R^2}} \\ & + 4\pi\sqrt{2\pi}\varepsilon \Big[\rho_{\text{h}}\sigma_{\text{h}} \exp\Big(-\frac{\sigma_{\text{h}}^2 u(q,R)^2}{2R^2}\Big) A(q, R - \Delta R, \sigma_{\text{h}}) \\ & + \rho_{\text{t}}\sigma_{\text{t}} \exp\Big(-\frac{\sigma_{\text{t}}^2 u(q,R)^2}{2R^2}\Big) A(q, R - \Delta R - \text{z}_{\text{hh}}/2, \sigma_{\text{t}}) \\ & + \rho_{\text{h}}\sigma_{\text{h}} \exp\Big(-\frac{\sigma_{\text{h}}^2 u(q,R)^2}{2R^2}\Big) A(q, R - \Delta R - \text{z}_{\text{hh}}, \sigma_{\text{h}})\Big], \end{aligned} \tag{2}$$

where $A(q, R, \sigma) = R^2 \sin(u(q, R))/u(q, R) + \sigma^2 \cos(u(q, R))$ and $u = qR\sqrt{\cos^2(\varphi) + \cos^2(\theta)\sin^2(\varphi) + \varepsilon^2\sin^2(\theta)\sin^2(\varphi)}$ have been defined for notational ease. For a detailed derivation of the form factors and approximations we refer to Supplementary Note 3.

Applying the same model to a powder-averaged sample, which is also polydisperse in both radius R and ellipticity ε, we obtain

$$\begin{aligned} I_{\text{poly}}(q) \quad = \quad & 2\pi\, r_0\, I_0 \Delta\Omega \rho_{\text{water}} \\ & \times \int_0^{\varepsilon_{\max}} P(\varepsilon) \int_{R_{\min}}^{R_{\max}} P(R) \int_0^{\frac{\pi}{2}} |F(q, R, \varepsilon, \theta)|^2 \sin(\theta)\, \mathrm{d}\varepsilon\, \mathrm{d}R\, \mathrm{d}\theta, \end{aligned} \tag{3}$$

with the probability density distributions $P(\varepsilon)$ for the ellipticity and $P(R)$ for the radius. Note that the integrand F is the same as in Eq.(2), but now for $u_{powder} = qR\sqrt{\sin^2(\theta) + \varepsilon^2\cos^2(\theta)}$.

Single vesicle fit

We first have to consider size and shape of the particles. The collected diffraction patterns do not exhibit a perfectly spherical shape, but show an

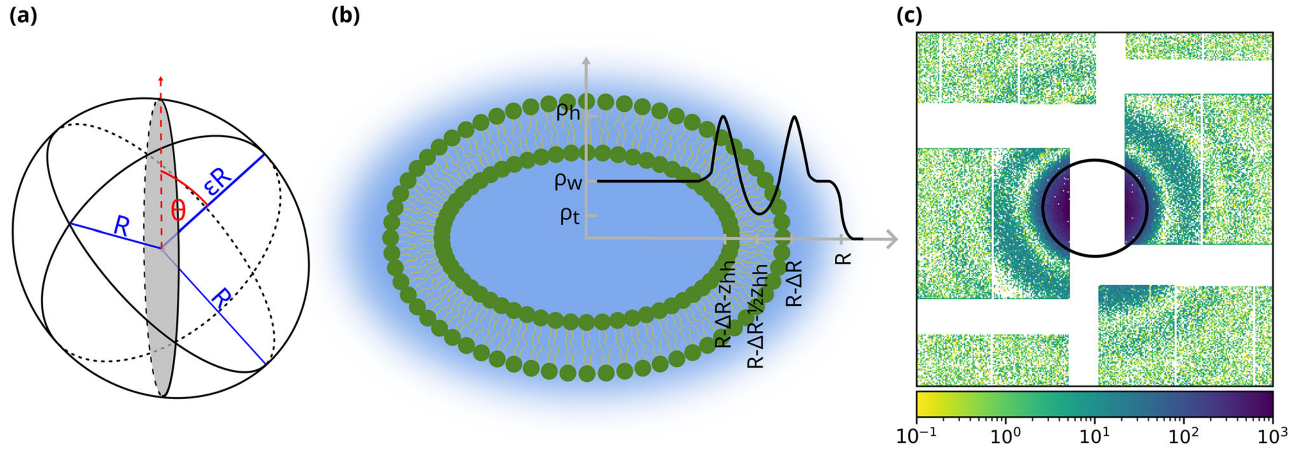

Fig. 3 | Fit model for single vesicle SAXS. a Schematic of an oblate ellipsoid with semi-axis R and ϵR. The angle θ describes the rotation perpendicular to the X-ray beam. **b** Schematic of an ellipsoidal lipid bilayer filled with water and surrounded by a thin water layer and corresponding electron density profile model. The electron density profile of the bilayer is described by three Gaussian functions, with electron densities ρ_h for the lipid head and ρ_t for the lipid chain regions. The electron density of the outside water layer is assumed to slowly decay. **c** Example of a 2D Gaussian fit to a diffraction pattern of a single lipid vesicle, collected in run 242, trainId 1329396439 and pulseId 32. The 2D ellipticity α is defined by the ratio between the lowest to highest width of the diffraction pattern.

elliptical deformation, reflecting an ellipsoidal deformation of the vesicles after aerosolization. We therefore describe the vesicles as oblate spheroids, see also Supplementary Note 1.7 for further justification. This shape transformation from spherical vesicles to ellipsoidal vesicles is likely to result from evaporation of excess water, and permeability of water from the vesicle lumen to the outside until cooling by evaporation slows down the process. At the same time, the results show that the hydrophilic head groups also of the outer lipid layer stay hydrated, i.e. a thin water layer remains on the vesicle surface. Second, the structure of the vesicle, in particular its radial density profile of the bilayer $\rho(r)$ has to be addressed. The usual approach to treat coherent diffractive data recorded from single particles is to invert the data by iterative phase retrieval algorithms which can solve the phase problem based on constraints[30,32,45]. In this way, 2D maps of the projected electron density can be obtained. However, for the present data this was not possible. The low signal and insufficient signal-to-noise towards the high q-range impeded faithful reconstruction of the bilayer profile, which requires single nanometer sensitivity. Another concern are also the relatively large inter-module gaps. In contrast to previous CDI studies of identical particles, we could not accumulate signal and increase resolution by averaging over multiple diffraction patterns without loss of information, due to the inherent polydispersity, of both radius and ellipticity. To still extract structural information of the single vesicles from the collected data, we therefore adopted a similar approach as in solution SAXS, using a suitable model function to fit the azimuthally averaged data of single lipid vesicles.

For fitting, diffraction patterns of single lipid vesicles obtained by automated hit-finding (see above) were further screened for those which exhibited a high point symmetry of the diffraction pattern (high Friedel score) and clearly distinguishable maxima and minima. The diffraction patterns were azimuthally averaged using the INTEGRATE1D function implemented in the PYFAI library[46]. Integration was performed in 1000 points along $q = \frac{4\pi}{\lambda}\sin(\gamma)$, the corresponding error was calculated using a Poissonian model. Dead pixels and modular gaps were masked using a pixel mask, that was calculated during data calibration. To find the starting conditions of the fit, two constrained least-square fits were performed, using simplified intensity models. This initial fitting process is described in Supplementary Note 3 in more detail. Since the error of the measured intensity in the low q-range seemed to be underestimated, the error in this range was multiplied by a factor of 5, accounting for possibly elevated systematic errors in this range. The exact q-range, in which this modification was performed varies between different data-sets, the exact values are tabulated in Tab. S1. The first 10 points ($0.0756\ \mathrm{nm}^{-1} \le q \le 0.1021\ \mathrm{nm}^{-1}$) were not included in the fit, since the signal was flawed by instrumental/detector noise. In fact, this artifact in the low q-range is caused by a saturation in this detector region due to too much intensity. This causes an automated switch in the detector gain and results in discontinuities in the measured signal. An unconstrained least-square fit using the previously described intensity model (Eq. (2)) was then performed on this data with partially modified error. Fitting was performed using the LSQNONLIN function implemented in the MATLAB R2020A (The MathWorks) optimization toolbox. The quality of the fit was monitored by the reduced χ^2 function

$$\chi^2_{\mathrm{red}} = \frac{1}{N-p-1}\sum_{i=1}^{N}\frac{(I_{\mathrm{exp}}(q_i) - I_{\mathrm{model}}(q_i))^2}{\sigma_i^2}, \tag{4}$$

with N the number of data-points, p the number of free model parameters and σ_i the standard deviation at data-point i of the measured curve I_{exp}. For this final step of the optimization, the trust-region-reflective algorithm was used. Figure 4 shows an example of such a fit, with (a) the azimuthally averaged intensity with super-imposed fit curve (red solid line) and χ^2_{red} given in the legend, and (b) the corresponding radial electron density profile $\rho(r)$. The roughness parameter σ converged towards 0, indicating a sharp outer interface between water and vacuum. Interestingly, however,if this parameter is not included in the model, the fit does not converge to realistic solutions. Note that while the presence of the bilayer and its qualitative shape is a robust result, we cannot claim unique solution in terms of precise parameters describing the bilayer profile. Similar but not identical solutions are found when varying the meta parameters optimization procedure, such as initial values, algorithms or parameter constraints.

Further scattering curves and corresponding results are shown in Figures S5–S9 of the Supplementary Information. The model parameters for all fits are tabulated in Tab. S5. Models assuming a spheroid water droplet without lipid bilayer gave substantially higher χ^2 values, failing to describe the data at moderate and high-q. We can therefore conclude that macromolecular resolution is obtained, i.e. a resolution high enough to identify the lipid bilayer and associated density profile. To achieve this, signal accumulation by azimuthal averaging was necessary. In this regard, it is also of interest to specify the resolution of a SAXS experiment given by the maximum scattering vector $q_{max} \simeq 3\ \mathrm{nm}^{-1}$ probed. Here we hence reach a resolution of $\pi/q = 1.05$ nm. However, within the priors of a model, structural parameters can be determined at an accuracy also below this value, since the model parameters of the electron density profile on sub-nm scale already influence the scattering curve at smaller $q \le q_{max}$. Moreover,

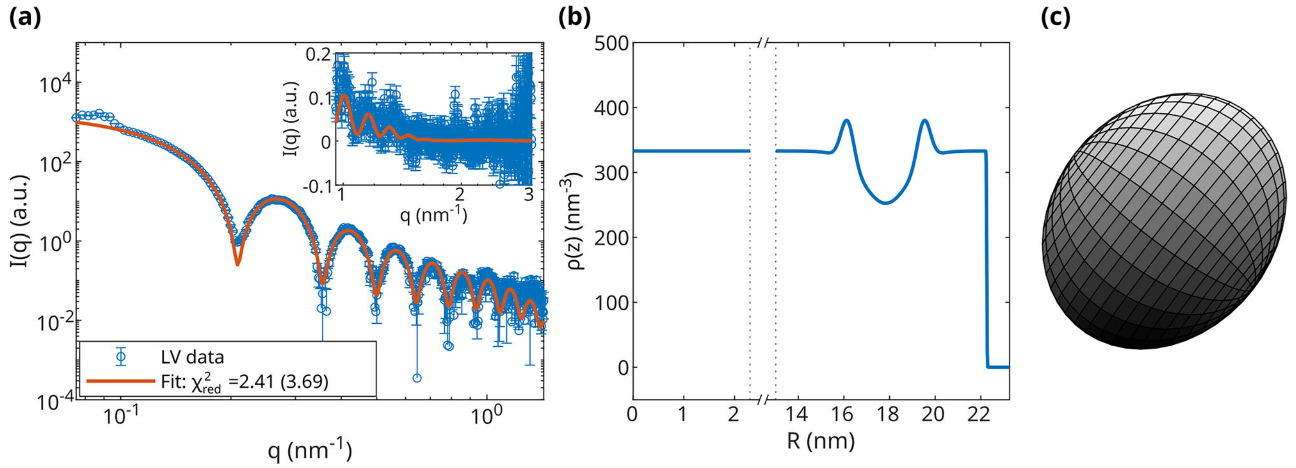

Fig. 4 | Least-square fit and electron density profile for a single vesicle. The data corresponds to event (hit) stamped as run 242/trainId 1329396439/pulseId 32. The corresponding diffraction pattern including a 2D Gaussian fit is shown in Fig. 3 (**c**). **a** Single vesicle SAXS curve (open blue circles) and least-square fit (solid red curve) using the single vesicle model described above. The error in low q is multiplied by a factor of 5 (see Tab. S1), to take into account systematic errors due to background subtraction and calibration. The χ^2_{red}- error is given in the legend, both for the modified error (without parentheses) and unmodified error (in parentheses). The inset shows data in the high q-range on a linear scale. **b** Radial electron density profile calculated from the model fit parameters derived in (**a**). **c** Ellipsoid corresponding to the fitted LV and surrounding water layer.

concerning the water shell we observed that a "soft" termination of the water shell of finite interfacial roughness σ helped the fits to converge, see Supplementary Information. Note that we model the water shell with constant thickness since we assume the hydrophilicity of the membrane surface to be homogeneous. Contrarily, for proteins, local variations of the hydration shell when injected into vacuum may reflect the local distribution of hydrophilic and hydrophobic amino acids[33].

Results and discussion

Batch analysis

To quantify the ensemble of all hits on single vesicles, the average vesicle radius R and average projected ellipticity α were calculated. To calculate the average vesicle radius, including the surrounding thin layer of water, the droplets were approximated as spherical particles. Thus the scattered intensity is described by $I_{\mathrm{sphere}} = |\frac{\sin(qR) - qR\cos(qR)}{(qR)^3}|^2$, which leads to the condition $q_{\mathrm{min}}R = \tan(q_{\mathrm{min}}R)$ for the positions of intensity minima q_{min}. Here, the position of the first intensity minimum was used to calculate the radius $R \approx \frac{4.493}{q_{\mathrm{min},1}}$. The resulting histogram is shown in Fig. 5(a). A lognormal distribution was fitted to the data, resulting in a mean R_μ = 18.32 nm and standard deviation σ = 5.16 nm. This is reasonable in view of the fact that the vesicles were extruded through a 50 nm pore membrane. To quantify the distribution of the ellipticity, we infer the 3D ellipticity of the spheroids from the distribution of the projected 2D ellipticities of the diffraction patterns, assuming isotropic distribution (no preferred orientation) of the spheroids. To this end, we first fitted a 2D Gaussian function to the diffraction patterns

$$G(x, y) = A[\exp\left(a(x - x_0)^2 + 2b(x - x_0)(y - y_0) + c(y - y_0)^2\right] + d, \tag{5}$$

where

$$\begin{aligned} a &= \frac{\cos^2(\varphi)}{2\sigma_x^2} + \frac{\sin^2(\varphi)}{2\sigma_y^2} \\ b &= -\frac{\sin(2\varphi)}{4\sigma_x^2} + \frac{\sin(2\varphi)}{4\sigma_y^2} \\ c &= \frac{\sin^2(\varphi)}{2\sigma_x^2} + \frac{\cos^2(\varphi)}{2\sigma_y^2}, \end{aligned} \tag{6}$$

with amplitude A, center (x_0, y_0), standard deviations of the semi-axis σ_x, σ_y, background d and angle in the detector plane φ. An example for such a Gaussian fit is shown in Fig. 3(c). The full-widths at half-maximum of the two semi-axis are given by $\mathrm{FWHM}_{x/y} = 2\sqrt{2\ln(2)}\sigma_{x/y}$. The projected 2D ellipticity α was then defined as

$$\alpha = \frac{\mathrm{FWHM}_{\mathrm{smaller}}}{\mathrm{FWHM}_{\mathrm{larger}}} < 1. \tag{7}$$

The resulting histogram of 2D ellipticities is shown in Fig. 5(b). Assuming oblate vesicles and a 3D ellipticity ε described by the shifted lognormal distribution

$$f(\varepsilon) = \frac{1}{\sqrt{2\pi}(1-\varepsilon)\sigma}\exp\left(-\frac{(\ln(1-\varepsilon)-\mu)^2}{2\sigma^2}\right), \tag{8}$$

with mean μ and standard deviation σ, the distribution of the 2D ellipticity is described by

$$f(\alpha, f(\varepsilon)) = \int_0^\alpha f(\varepsilon) f_\alpha(\alpha, \varepsilon)\mathrm{d}\varepsilon\,, \tag{9}$$

with the distribution of the 2D ellipticities for a given 3D ellipticity

$$f_\alpha(\alpha, \varepsilon) = \frac{\alpha}{\sqrt{(1-\varepsilon^2)(\alpha^2-\varepsilon^2)}}. \tag{10}$$

This was fitted to the data using the lsqnonlin-function and a Levenberg-Marquardt algorithm. The quality of fit was monitored by a χ^2 − function. The resulting fit to the 2D ellipticities α as well as the resulting distribution of the 3D ellipticities ε, with mode = 0.86, standard deviation σ = 0.08 and mean = 0.82, are shown in Fig. 5(b). Considering the mode of the obtained distribution, corresponding to an oblate spheroid with ε = 0.86, we obtain a volume shrinkage of 0.623%. Note that we expect a spherical shape to be most probable after preparing the vesicles by extrusion. However, the vesicles are aerosolized and excess water may not only have evaporated from the outside but also from the lumen of the vesicle, given the membrane permeability. A resulting shape transformation due to a slight mismatch between the surface and the volume may then explain the oblate shape. The evidence for a prolate rather than an oblate shape, derives from the fact that least-squares fits of an oblate ellipsoid to the histogram produces a lower χ^2 than a prolate ellipsoid (see Fig. S3, Supplementary Information). Since, the models for prolate and oblate shapes only differ in the wings of the distribution, we cannot rule out a selection bias or a bimodal distribution of oblate and prolate shapes, for example due to a possible excitation of

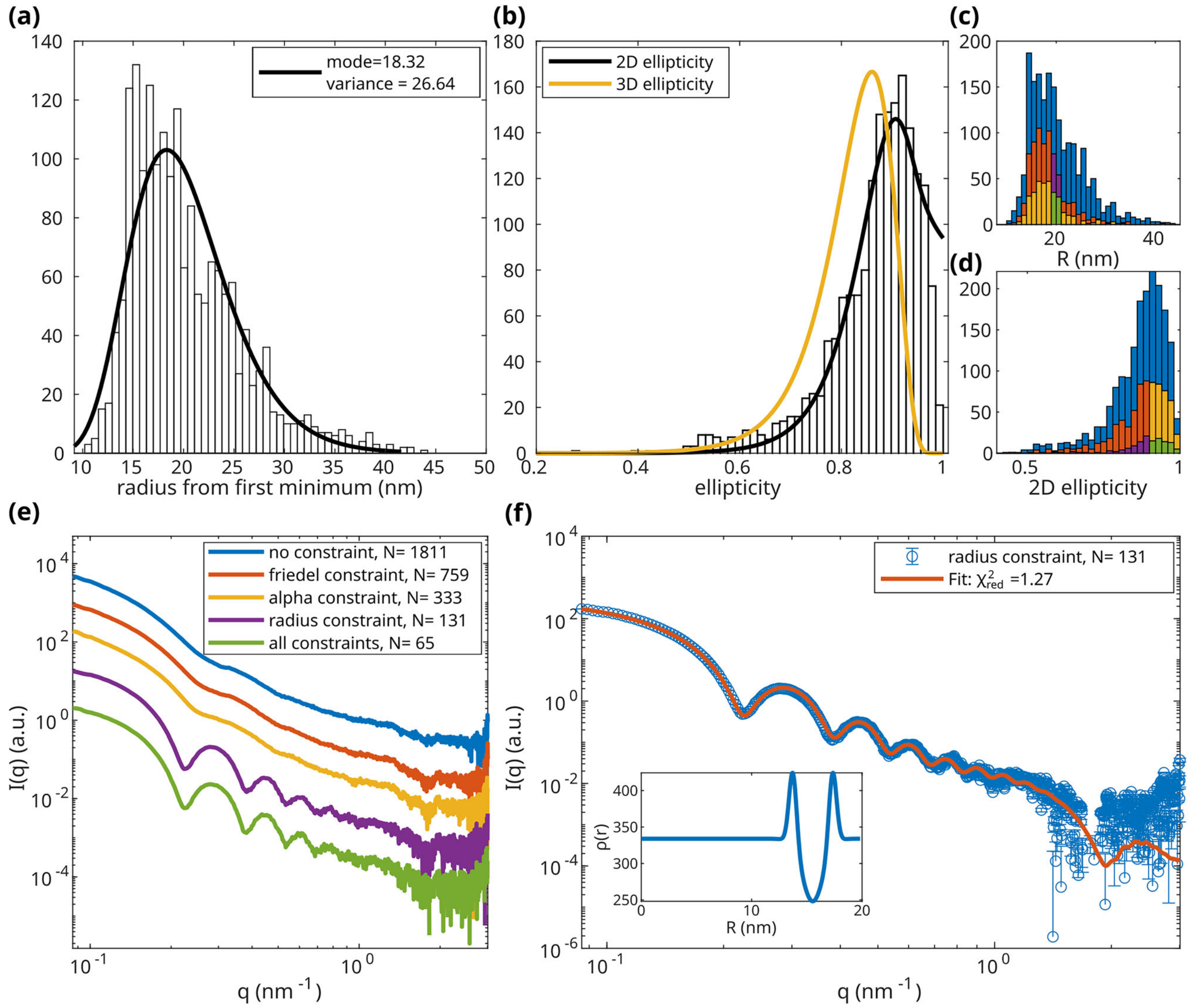

Fig. 5 | Batch processing and in silico purification of vesicle hits. a Distribution of radii resulting from the position of the first minimum collected on multiple runs on lipid vesicles. $N = 1811$ single vesicle hits were found. A lognormal distribution was fitted to the data. **b** Distribution of the 2D ellipticity α obtained from 2D Gaussian fits to the diffraction patterns. Assuming a lognormal distribution for the 3D ellipticity ε and oblate vesicle geometry, an estimate of α (black curve) and ε (yellow curve) was calculated. The best fit resulted in a 3D distribution with $mode = 0.86$, standard deviation $\sigma = 0.08$, and $mean = 0.82$. **c**, **d** Distributions of radii and 2D ellipticity for different purification constraints. The color-scheme is shown in (**e**). **e** Resulting averaged scattered intensity resulting from the different constraints. The curves were shifted for clarity. (**f**) Background subtracted scattered intensity resulting from the radius constraint, averaging over $N = 131$ hits. The errors correspond to the empirical error of the mean, for each q. The solid line represents the least-squared fit using the powder-averaged intensity model. The radius was described by a uniform distribution, while the 3D ellipticity was described by a lognormal distribution with values obtained from the fit to the 2D ellipticity distribution. The radius was varied freely, while the ellipticity was kept constant. The radius was sampled with 10 points, the ellipticity with 30. The corresponding model fit parameters are shown in Table 2. The inset shows the corresponding electron density profile.

oscillations between oblate and prolate shapes in the course of aerosolization. Note that the equilibrium phase diagram of vesicles for a reduced volume slightly below one, would favor a prolate shape[47].

In Silico Purification

With these distributions of radii and projected ellipticity, it is now possible to create in-silico purified powder-averaged data by averaging over diffraction patterns of vesicles with similar properties. This was carried out for a set of different properties. The resulting histograms for radius and ellipticity are shown in Fig. 5(c), (d), respectively. The corresponding averaged scattering curves are shown in (e). The data labeled 'no constraints' comprises all data, that was classified as hits. The curve labeled "Friedel constraint" refers to data with a Friedel score $f > 0.8$, i.e. data with high symmetry and good signal-to-noise ratio. The "alpha-constraint" refers to data with $f > 0.8$ and 2D ellipticities of $0.8 \le \alpha \le 1$, and the "radius constraint" denotes data with $f > 0.8$ and radii of $19\ \mathrm{nm} \le R \le 21\ \mathrm{nm}$, while 'all constraints' only corresponds to data that fulfills all of the constraints above. Please note that these curves differ from the classical solution scattering curves for lipid vesicles as shown for example in refs. 12, 15, because even though the vesicles are still hydrated in the presented measurements, the electron density profile is dominated by the interface between water and air. Nevertheless all curves show 1–2 more or less pronounced modulations (maxima/minima) in the range $1\ \mathrm{nm}^{-1} \le q \le 2.5\ \mathrm{nm}^{-1}$, which are associated with the lipid bilayer. The modulations are most prominent in the radius constrained data. In the lower q-range the curves with no constraint, Friedel constraint and alpha constraint (blue, red and yellow) exhibit the same characteristic modulations without distinguishable maxima and minima. Contrarily, the curve with a radius constraint (purple) and all constraints (green) show the clearly visible characteristic maxima and minima of spherical or elliptical particles. This shows, that even though both polydispersities (ε and R) influence the

Table 2 | Parameters resulting from the least-square fits to the single lipid vesicle (stamped run 242/trainId 1329396439/pulseId 32) using the single vesicle model and the fit to the purified curve with radius constraint using the model for powder-averaged lipid vesicles

Model parameter	single vesicle run 242, 32	radius constraint purification	unit
R	22.26	–	nm
R_{lower}	–	19.82	nm
R_{upper}	–	22.32	nm
ε	0.82	–	–
μ_{ε}	–	-1.98	–
σ_{ε}	–	0.299	–
$\cos(\theta)$	0.83	–	–
z_{hh}	3.35	3.6	nm
ρ_{h}	0.2	0.31	nm^{-1}
ρ_{t}	-0.24	-0.26	nm^{-1}
σ_{h}	0.28	0.35	–
σ_{t}	1.01	0.96	–
ΔR	2.76	2.5	nm
scale $\cdot 10^{7}$	2.03	5.74	a.u.
$\sigma \cdot 10^{3}$	15.14	–	–

For the purified curve, the radius was described by a uniform distribution between R_{lower} and R_{upper}. The 3D ellipticity ε is described by a lognormal distribution with mean μ_{ε} and standard deviation σ_{ε}, these values were kept constant at values derived from the 2D ellipticity.

scattered intensity, the polydispersity in the radius seems to have a stronger effect of averaging out the characteristic modulations. Note that in the preparation protocol, sonication before extrusion could possibly give a narrower size distribution. However, the SP-SAXS method does not depend on a particularly small polydispersity for structural analysis, and works also well for a broader distribution as here. This is particularly relevant for applications of samples with delicate composition such as proteo-liposomes, where sonication could potentially induce harm.

Similar to the single vesicle curves, the structural information of the scattering vesicles are extracted from the quasi powder-averaged purified curves by fitting a suitable model function. This is exemplified for the curve resulting from the radius constraint. For fitting, the model for powder-averaged lipid vesicles was used. The radius was described by a uniform distribution, which was sampled along 10 points. The 3D ellipticity was described by the lognormal distribution resulting from a fit to the radius-constrained 2D ellipticity distribution using Eq.(10). The distribution was kept constant during the fitting process and was sampled along 30 points. Fitting was implemented as described for the single vesicles. However, in contrast to the single vesicle fit, no surface roughness of the bound water layer was assumed. Fitting was performed in a range between $0.28\ \mathrm{nm}^{-1} \leq q \leq 3\ \mathrm{nm}^{-1}$. The resulting fit and corresponding $\chi^2_{\mathrm{red}}-$ error is shown in Fig. 5(f), the resulting model fit parameters in Table 2. The parameters corresponding to the lipid bilayer, and the thickness ΔR of the thin water layer on the outside of the vesicles, match those found in single vesicle fits (compare Table 2), resulting in a similar electron density profile as visualized in the inset.

Conclusion

We have demonstrated structural analysis of lipid vesicles as a prototype of many related problems at the single particle level, exploiting extreme concentration of X-ray photons in space and time. This warrants a sufficient signal level and at the same time helps to circumvent radiation damage based on the *diffract-before-destroy* principle. The single particle diffraction data was analyzed similar to solution SAXS data, by fitting a suitable form factor, but without the ensemble average inherent in conventional SAXS. Instead of averages for vesicle radius R, ellipticity ε and the radial electron density profile $\rho(r)$, we obtain these structural parameters for each vesicle, possibly for each of 10^6 diffraction patterns recorded within each run of about 5 min. Given the stochastic nature of the vesicle injection and missed overlap in space and time, only 0.01% of the recorded diffraction images can be classified as 'good hits'. Based on automated batch analysis, further constraints can be applied, adopting a strategy of in-silico purification, for example to accumulate data for vesicles which fall into a given interval of radii or ellipticity values. At the same time we get direct and independent information on the distribution functions $P(R)$ and $P(\varepsilon)$, in particular since R and ε can be inferred directly from the diffraction data even without a full q-range fit to a model with many parameters. Two different advantages follow from this form of serial single particle SAXS: 1.) One can create SAXS curves of 'artificial ensembles' with accumulated signal, while at the same time controlling the polydispersity or even achieving quasi-monodisperse ensembles. In this way the overall screening effect which polydispersity has on many structural details is reduced, and more complicated colloidal or macromolecular assemblies or biological particles can become accessible. 2.) We can precisely measure polydispersity functions (distribution functions), which is relevant in view of the self-assembly process, synthesis and/or biological or material function. Note that while the width of the distribution is a parameter accessible by ensemble fitting, the detailed functional shape is much more elusive in conventional SAXS.

How should we delineate the present approach from the stated goals of 'diffractive imaging' based on phase retrieval and model independent inversion of the diffraction data, representing the original goal of CDI? Of course, a diffraction model can also be regarded as an extreme form of a real-space constraint, reducing say some 10^6 independent unknowns in an image by say a dozen structural parameters. While loosing generality in this way, it is obvious that the latter makes the analysis more robust and increases the compatibility with many experimental conditions, in view of signal strength and sampling issues. In the present case, where each particle is different, the signal cannot be accumulated over many shots. And even if the signal of a single image would be high enough, the detection must also fulfill tighter sampling constraints compared to SP-SAXS. Another major difference is the fact, that CDI inverts the diffraction pattern to a 2D image of the projected electron density, while SAXS models are intrinsically based on formulating a structure directly in 3D. This is of significant advantage when only a single image for each (different) particle is available. Hence, it is justified to conclude that SP-SAXS provides complementary structural information, even in cases where CDI-based (shape) reconstruction would in principle be possible. However, improvements in classification and reconstruction algorithms may help to overcome these limitations due to the particles being possibly in many different states or conformations. Approaches based on Bayesian analysis[39], machine learning[34], and generalization of phase retrieval to ensembles[48] all represent very promising directions.

Aside from analysis, both XFEL generation and optics, as well as detectors hold tremendous potential for further improvements. XFEL seeding in particular, can help to increase the hit rate, and to better exploit the signal level for analysis, since the typical SASE fluctuations are suppressed. Note that the self-amplified spontaneous emission (SASE) process is associated with strong pulse-to-pulse fluctuations, not only in intensity, but also in phase and pulse shape, which affects pulse propagation through the beamline optics and in particular the nano-focusing. Pointing stability and efficiency of focusing could be be improved by seeding, resulting in a deterministic pulse generation process, even at the expense of reduced average flux. Ultimately, also the recent demonstration of a Free Electron Laser Oscillator[49] could substantially benefit the hit rate and overall performance of SP-SAXS. The weakest point in the current work, however, is arguably not related to the beam or the detection, but the sample injection. We do not yet sufficiently control the aerosolization process or even know to which temperature the particle cools down by evaporational cooling. The observed ellipticity distribution is too broad to represent a thermal state, and also unlikely to result from the vesicle preparation. Instead, we must attribute this result to a shape transformation from spherical vesicles to ellipsoidal vesicles due to evaporation of excess water. This goes along with partial transport of water from the lumen to the outer surface, since the membrane is partially permeable for water. This process may eventually be stopped by evaporational cooling and the resulting shape freezes in. Here we observe an outer water layer around the bilayer likely to be tightly coordinated to the lipid headgroups (bound water). Given the fact that the hydration shell for lipid bilayers is thicker than for most amino acids, we can assume that the thin water shell is smooth and less corrugated than that of most proteins injected into vacuum under similar conditions[33]. For vesicles, the hydration shell may hence serve as a protective layer. Nevertheless, a more controlled and less invasive injection process is desirable.

Furthermore, the strong dominating signal from the interface between the outside water layer and the air surrounding the vesicle containing droplet, compared to the scattering from within the droplet, can also present a challenge (see also Supplementary Note 3). Recent experiments using water sheet jet injectors producing sheet jets with thicknesses below 100 nm demonstrated that data collection was possible for near MHz repetition rates[50]. These jets could also be used for single particle SAXS and may lead to an improvement of visibility of the biomolecular diffraction signal. Notwithstanding these challenges, even with the current setup, we were already able to inject also more complex and potentially more fragile biological vesicles, notably synaptic vesicles as well as vesicles with reconstituted proteins (proteo-liposomes), without indication of damage by the aerosol process. Finally, given the considerable experimental efforts already made, it seems very reasonable to capitalize on this method development and to extend the research from structural analysis of simple and in future more complex colloidal biological particles, also to *structural dynamics*, based on two consecutive pulses, an optical pump pulse and a delayed single XFEL probing pulse. Photochemical reactions and transition of single particles should then become uniquely accessible. Also for this direction, the single particle SAXS approach shown here seems very promising.

Data availability

Data recorded for the experiment at the European XFEL are available at doi:10.22003/XFEL.EU-DATA-002812-00.

Code availability

The algorithms used to reproduce the findings of this study are described in detail within the manuscript and the Methods. The code is available from the corresponding author upon request.

Received: 26 September 2025; Accepted: 10 February 2026;

References

1. Debye, P. & Scherrer, P. Interferenzen an regellos orientierten Teilchen im Röntgenlicht. ii. *Nachr. von Ges. Wiss. Gött. Math.-Phys. Kl* **1916**, 16–26 (1916).
2. Bremholm, M., Felicissimo, M. & Iversen, B. B. Time-resolved in situ synchrotron x-ray study and large-scale production of magnetite nanoparticles in supercritical water. *Angew. Chem.* **121**, 4882–4885 (2009).
3. Sun, Y. Anomalous small-angle X-ray scattering for materials chemistry. *Trends Chem.* **3**, 1045–1060 (2021).
4. Li, T., Senesi, A. J. & Lee, B. Small angle x-ray scattering for nanoparticle research. *Chem. Rev.* **116**, 11128–11180 (2016).
5. Derry, M. J., Mykhaylyk, O. O. & Armes, S. P. A vesicle-to-worm transition provides a new high-temperature oil thickening mechanism. *Angew. Chem.* **129**, 1772–1776 (2017).
6. Chagri, S., Ng, D. Y. W. & Weil, T. Designing bioresponsive nanomaterials for intracellular self-assembly. *Nat. Rev. Chem.* **6**, 320–338 (2022).
7. Hollamby, M. J. et al. Simultaneous SAXS and SANS analysis for the detection of toroidal supramolecular polymers composed of noncovalent supermacrocycles in solution. *Angew. Chem.* **128**, 10044–10047 (2016).
8. Angelova, A., Angelov, B., Mutafchieva, R., Lesieur, S. & Couvreur, P. Self-assembled multicompartment liquid crystalline lipid carriers for protein, peptide, and nucleic acid drug delivery. *Acc. Chem. Res.* **44**, 147–156 (2011).
9. Safinya, C. R. & Rädler, J. O.*Handbook of Lipid Membranes: Molecular, Functional, and Materials Aspects* (CRC Press, 2021).
10. Brzustowicz, M. R. & Brunger, A. T. X-ray scattering from unilamellar lipid vesicles. *J. Appl. Crystallogr.* **38**, 126–131 (2005).
11. Kučerka, N., Nieh, M.-P. & Katsaras, J. Fluid phase lipid areas and bilayer thicknesses of commonly used phosphatidylcholines as a function of temperature. *Biochim. et. Biophys. Acta (BBA) Biomembr.* **1808**, 2761–2771 (2011).
12. Konarev, P. V., Gruzinov, A. Y., Mertens, H. D. T. & Svergun, D. I. Restoring structural parameters of lipid mixtures from small-angle X-ray scattering data. *J. Appl. Crystallogr.* **54**, 169–179 (2021).
13. Bouwstra, J., Gooris, G., Bras, W. & Talsma, H. Small angle X-ray scattering: possibilities and limitations in characterization of vesicles. *Chem. Phys. Lipids* **64**, 83–98 (1993).
14. Šegota, S. & Težak, D. Spontaneous formation of vesicles. *Adv. Colloid Interface Sci.* **121**, 51–75 (2006).
15. Komorowski, K. et al. Vesicle adhesion and fusion studied by small-angle X-ray scattering. *Biophys. J.* **114**, 1908–1920 (2018).
16. Pabst, G. & Keller, S. Exploring membrane asymmetry and its effects on membrane proteins. *Trends Biochem. Sci.* **49**, 333–345 (2024).
17. Winter, R. & Jeworrek, C. Effect of pressure on membranes. *Soft Matter* **5**, 3157–3173 (2009).
18. Trollmann, M. F. & Böckmann, R. A. mRNA lipid nanoparticle phase transition. *Biophys. J.* **121**, 3927–3939 (2022).
19. Komorowski, K. et al. Neurotransmitter uptake of synaptic vesicles studied by X-ray diffraction. *Eur. Biophys. J.* **51**, 465–482 (2022).
20. Neutze, R., Wouts, R., Van der Spoel, D., Weckert, E. & Hajdu, J. Potential for biomolecular imaging with femtosecond X-ray pulses. *Nature* **406**, 752–757 (2000).
21. Chapman, H. N. et al. Femtosecond diffractive imaging with a soft-X-ray free-electron laser. *Nat. Phys.* **2**, 839–843 (2006).
22. Sun, Z., Fan, J., Li, H. & Jiang, H. Current status of single particle imaging with X-ray lasers. *Appl. Sci.* **8**, 132 (2018).
23. Bielecki, J., Maia, F. R. N. C. & Mancuso, A. P. Perspectives on single particle imaging with X-rays at the advent of high repetition rate X-ray free electron laser sources. *Struct. Dyn.* **7**, 040901 (2020).
24. Miao, J., Charalambous, P., Kirz, J. & Sayre, D. Extending the methodology of X-ray crystallography to allow imaging of micrometre-sized non-crystalline specimens. *Nature* **400**, 342–344 (1999).
25. Miao, J., Ishikawa, T., Robinson, I. K. & Murnane, M. M. Beyond crystallography: diffractive imaging using coherent X-ray light sources. *Science* **348**, 530–535 (2015).
26. Berberich, T. B., Molodtsov, S. L. & Kurta, R. P. A workflow for single-particle structure determination via iterative phasing of rotational invariants in fluctuation X-ray scattering. *J. Appl. Crystallogr.* **57**, 324–343 (2024).
27. Sobolev, E. et al. Megahertz single-particle imaging at the European XFEL. *Commun. Phys.* **3**, 97 (2020).
28. Mancuso, A. P. et al. The single particles, clusters and biomolecules and serial femtosecond crystallography instrument of the {European XFEL}: initial installation. *J. Synchrotron Radiat.* **26**, 660–676 (2019).
29. Bielecki, J. et al. Electrospray sample injection for single-particle imaging with x-ray lasers. *Sci. Adv.* **5**, eaav8801 (2019).
30. Seibert, M. M. et al. Single mimivirus particles intercepted and imaged with an X-ray laser. *Nature* **470**, 78–81 (2011).
31. Ekeberg, T. et al. Three-dimensional reconstruction of the giant mimivirus particle with an X-Ray free-electron laser. *Phys. Rev. Lett.* **114**, 098102 (2015).

32. Hantke, M. F. et al. High-throughput imaging of heterogeneous cell organelles with an X-ray laser. *Nat. Photonics* **8**, 943–949 (2014).
33. Ekeberg, T. et al. Observation of a single protein by ultrafast X-ray diffraction. *Light Sci. Appl.* **13**, 15 (2024).
34. Hu, M., Fan, J., Tong, Y., Sun, Z. & Jiang, H. Deep learning for ultrafast X-ray scattering and imaging with intense X-ray FEL pulses. *Adv. Opt. Technol.* **14**, 1546386 (2025).
35. Chapman, H. N. X-ray free-electron lasers for the structure and dynamics of macromolecules. *Annu. Rev. Biochem.* **88**, 35–58 (2019).
36. Brändén, G. et al. Coherent diffractive imaging of microtubules using an X-ray laser. *Nat. Commun.* **10**, 2589 (2019).
37. Oberthür, D. Biological single-particle imaging using XFELs – towards the next resolution revolution. *IUCrJ* **5**, 663–666 (2018).
38. Walczak, M. & Grubmüller, H. Bayesian orientation estimate and structure information from sparse single-molecule x-ray diffraction images. *Phys. Rev. E* **90**, 022714 (2014).
39. Schultze, S. & Grubmüller, H. Bayesian electron density determination from sparse and noisy single-molecule X-ray scattering images. *Sci. Adv.* **10**, eadp4425 (2024).
40. Blanchet, C. E. et al. Form factor determination of biological molecules with X-ray free electron laser small-angle scattering (XFEL-SAS). *Commun. Biol.* **6**, 1057 (2023).
41. Abeghyan, S. et al. First operation of the SASE1 undulator system of the European X-ray Free-Electron Laser. *J. Synchrotron Radiat.* **26**, 302–310 (2019).
42. Maltezopoulos, T. et al. Operation of x-ray gas monitors at the {European XFEL}. *J. Synchrotron Radiat.* **26**, 1045–1051 (2019).
43. Allahgholi, A. et al. The adaptive gain integrating pixel detector at the {European XFEL}. *J. Synchrotron Radiat.* **26**, 74–82 (2019).
44. Pabst, G., Rappolt, M., Amenitsch, H. & Laggner, P. Structural information from multilamellar liposomes at full hydration: full q-range fitting with high quality x-ray data. *Phys. Rev. E* **62**, 4000–4009 (2000).
45. Miyashita, O. & Joti, Y. X-ray free electron laser single-particle analysis for biological systems. *Curr. Opin. Struct. Biol.* **43**, 163–169 (2017).
46. Kieffer, J., Valls, V., Blanc, N. & Hennig, C. New tools for calibrating diffraction setups. *J. Synchrotron Radiat.* **27**, 558–566 (2020).
47. Seifert, U. Configurations of fluid membranes and vesicles. *Adv. Phys.* **46**, 13–137 (1997).
48. Shen, Z. et al. Resolving nonequilibrium shape variations among millions of gold nanoparticles. *ACS Nano* **18**, 15576–15589 (2024).
49. Rauer, P. et al. Lasing of a cavity-based X-ray source. *Nature* **650**, 93–96 (2026).
50. Konold, P. E. et al. 3D-printed sheet jet for stable megahertz liquid sample delivery at X-ray free-electron lasers. *IUCrJ* **10**, 662–670 (2023).
51. {European XFEL}. Spb/sfx instrument design. https://www.xfel.eu/facility/instruments/spb_sfx/instrument_design/index_eng.html (2024).
52. Luebke, J. *Control of Bionanoparticles with Electric Fields*. Dissertation, Universität Hamburg (2023).
53. Hantke, M. F. et al. Rayleigh-scattering microscopy for tracking and sizing nanoparticles in focused aerosol beams. *IUCrJ* **5**, 673–680 (2018).

Acknowledgements

We acknowledge European XFEL in Schenefeld, Germany, for provision of X-ray free-electron laser beamtime at Scientific Instrument SPB/SFX (Single Particles, Clusters, and Biomolecules and Serial Femtosecond Crystallography) under proposal number 2812 and would like to thank the entire staff for excellent working conditions. The project is funded through grant SFB1286/A2 (*Quantitative Synaptology*) of the German science foundation (DFG). Additional support came from the German Ministry of research (BMFTR) through the ERuM-Pro program/project 05K22MG2. A.M. and T.S. are members of the Max-Planck School Matter-to-Life. This research was supported in part through the Maxwell computational resources operated at Deutsches Elektronen-Synchrotron DESY, Hamburg, Germany.

Author contributions

C.N. and T.S. designed research. C.N., K.K. and J.A. prepared samples, J.B. and S.R.-Z. devised protocols and tools for sample injection. R.B., J.B., R.d.W. and R.L. operated the SPB instrument. All authors participated in the XFEL experiments and/or contributed experimental tools. C.N., M.S. analyzed data with input from M.O. and T.S. Further technical input was provided from J.E. and A.M. C.N. and T.S. wrote the manuscript; all authors proofread the manuscript. T.S. was PI of associated funding and beamtime applications.

Funding

Open Access funding enabled and organized by Projekt DEAL.

Competing interests

The authors declare no competing interests.

Additional information

Supplementary information The online version contains supplementary material available at https://doi.org/10.1038/s42005-026-02551-5.

Correspondence and requests for materials should be addressed to Tim Salditt.

Peer review information *Communications Physics* thanks Akihiro Suzuki and the other, anonymous, reviewer(s) for their contribution to the peer review of this work. [A peer review file is available.]